

RESEARCH ARTICLE

10.1002/2015JC011516

Key Points:

- Observations of low-frequency motions on steep fringing reefs exhibit modal behavior
- A linear model with forcing derived from a point-break model of setup describes the observations
- Reefs with larger dissipative than inertial time scales exhibit more low-frequency variability

Correspondence to:

J. M. Becker,
jbecker@soest.hawaii.edu

Citation:

Becker, J. M., M. A. Merrifield, and H. Yoon (2016), Infragravity waves on fringing reefs in the tropical Pacific: Dynamic setup, *J. Geophys. Res. Oceans*, 121, 3010–3028, doi:10.1002/2015JC011516.

Received 1 FEB 2016

Accepted 4 APR 2016

Accepted article online 7 APR 2016

Published online 13 MAY 2016

Infragravity waves on fringing reefs in the tropical Pacific: Dynamic setup

J. M. Becker¹, M. A. Merrifield², and H. Yoon²
¹Department of Geology and Geophysics, School of Ocean and Earth Science and Technology, University of Hawai'i at Mānoa, Honolulu, Hawaii, USA, ²Department of Oceanography, School of Ocean and Earth Science and Technology, University of Hawai'i at Mānoa, Honolulu, Hawaii, USA

Abstract Cross-shore pressure and current observations from four fringing reefs of lengths ranging from 135 to 420 m reveal energetic low-frequency (~ 0.001 – 0.05 Hz) motions. The spatial structure and temporal amplitudes of an empirical orthogonal function analysis of the pressure measurements suggest the dominant low-frequency variability is modal. Incoming and outgoing linear flux estimates also support partially standing modes on the reef flat during energetic events. A cross-covariance analysis suggests that breakpoint forcing excites these partially standing modes, similar to previous findings at other steep reefs. The dynamics of Symonds *et al.* (1982) with damping are applied to a step reef, with forcing obtained by extending a point break model of Vetter *et al.* (2010) for breaking wave setup to the low-frequency band using the shoaled envelope of the incident free surface elevation. A one parameter, linear analytical model for the reef flat free surface elevation is presented, which describes between 75% and 97% of the variance of the observed low-frequency shoreline significant wave height for all reefs considered over a range of conditions. The linear model contains a single dimensionless parameter that is the ratio of the inertial to dissipative time scales, and the observations from this study exhibit more low-frequency variability when the dissipative time scale is greater than the inertial time scale for the steep reefs considered.

1. Introduction

Motions in the low-frequency (here $0.001 < f < 0.05$ Hz) or infragravity (IG) band have been shown to be an important component of reef flat hydrodynamics in observational studies [Nakaza and Hino, 1991; Lugo-Fernandez *et al.*, 1998; Pequignet *et al.*, 2009; Pomeroy *et al.*, 2012; Torres-Freyermuth *et al.*, 2012; Pequignet *et al.*, 2014], and in laboratory experiments and numerical simulations [Nwogu and Demirbilek, 2010; Yao *et al.*, 2012; Van Dongeren *et al.*, 2013; Ma *et al.*, 2014; Su *et al.*, 2015]. In particular, inundation events at low-lying atolls and islands have been observed where the contribution to the shoreline water level is dominated by these low-frequency motions [Ford *et al.*, 2012; Sheremet *et al.*, 2014; Merrifield *et al.*, 2014]. Merrifield *et al.* [2014] applied a forced, damped oscillator equation to IG reef flat motions at two sites in the Republic of the Marshall Islands and found significant correlation between observed and modeled IG wave heights.

On steep fringing reefs, these low-frequency motions may be generated by breakpoint forcing [e.g., Pomeroy *et al.*, 2012; Pequignet *et al.*, 2014]. Breakpoint forcing first was shown theoretically to generate IG motions on planar beaches by Symonds *et al.* [1982]. Here, we apply the dynamics of Symonds *et al.* [1982] to an idealized step reef with breakpoint forcing due to dynamic setup. Dynamic setup follows from the equations of steady setup with the addition of the time varying surface elevation in the continuity equation and acceleration in the momentum equation [Lo, 1988]. For a fringing reef with a steep reef face, Vetter *et al.* [2010] used a point break assumption in a simple model of reef flat setup. We extend the point break model of setup to the IG band and use insights (and empirical parameters) from the setup analysis of Becker *et al.* [2014] for the time-dependent breakpoint forcing.

We use observations on four fringing reefs to describe the low-frequency variability and to motivate the simple forced oscillator equation presented here and applied in Merrifield *et al.* [2014]. We also present a linear forced, damped long wave equation that governs the dynamics of the reef flat IG motions from which the forced oscillator equation was obtained, and apply the model to two additional fringing reefs.

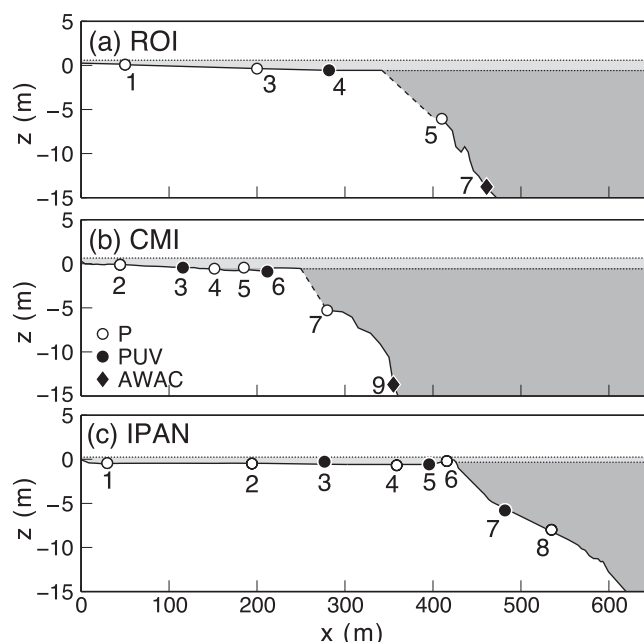


Figure 1. Bathymetry and sensor positions for the data sets described in Table 1 for ROI, CMI, and IPAN. The band of water levels at the surface represents mean lower low and higher high water levels computed for the duration of the ROI, CMI, and IPL deployments.

considered here are atoll islands in the Republic of the Marshall Islands. Site 1 (ROI) is located on Kwajalein atoll where a cross-shore instrument array aligned along $\sim 20^\circ\text{N}$ (N is true north and positive angles are clockwise throughout) was deployed on the north side of Roi-Namur at the northern tip of Kwajalein. Site 2 (CMI) is located on Majuro atoll where a sensor array, aligned $\sim 50^\circ\text{N}$, was deployed on the fringing reef adjacent to the College of the Marshall Islands. Details of the sites at ROI and CMI are described in *Becker et al.* [2014]. Site 3 (IP) is located at Ipan reef where various cross-shore instrument arrays have been deployed from August 2005–present on the southeast side of Guam. We here use deployments IPG (June–July 2007), IPL (December 2008 to February 2009), and IPN (August–November 2009) for site 3. Site 4 (SAI) is Laulau Bay, Saipan, where two pressure sensors were deployed from June to July 2007 during tropical storm ManYi. Sites IP and SAI are described in *Vetter et al.* [2010]. The reef lengths of ROI, CMI, IP, and SAI are ~ 350 , 220, 420, and 135 m, respectively.

The cross-shore arrays at each of the study sites consist of bottom-mounted pressure sensors (Sea-Bird SBE26plus) and combined pressure sensors and acoustic Doppler current profilers (Nortek Aquadopp) (Figure 1 for ROI, CMI, IP, detailed bathymetry is not available for SAI). The array details and sampling schemes may be found in *Becker et al.* [2014] for ROI, CMI, and IPL and IPN, and in *Vetter et al.* [2010] for IPG and SAI. All data were sampled at 1 Hz, and the length of record analyzed here is determined either by the longest record available or a subrecord long enough to resolve the low-frequency band (for IPG and SAI, we subdivide the 43180 s records into 7196 s records). Table 1 describes the instruments and pressure and current records used in the present analysis. Pressure records with less than 0.1 m of water over a sensor are not considered in our analysis. Current data for which backscatter amplitudes fall below a threshold are eliminated from the analysis, which correspond to records with low water levels.

Sea surface elevation time series are obtained using linear theory to depth correct the detided records of bottom pressure. The significant wave height is 4σ , where σ is the standard deviation of the band-passed surface elevation. The IG band is defined as frequencies between $0.0011 < f < 0.033$ Hz for ROI and CMI, and between $0.001 < f < 0.05$ Hz for IP and SAI. We choose slightly different low-frequency bands for the sites to avoid contamination from the sea and swell band and to be consistent with previous studies [*Pequignat et al.*, 2014].

The IG significant wave heights, H_{ig} , at the closest instrument to the shore ($x_s = 50$, 44, 30, and 68 m for sites 1–4, respectively, see Table 1) are compared to the incident (reef face) significant wave height in the sea

Nondimensionalizing the long wave equation provides a single parameter, $\delta = \mathcal{D}L / \sqrt{gh_r}$, that is the ratio of the inertial to dissipative time scales where \mathcal{D} is a constant linear dissipation rate, L is the reef length, g is gravity, and h_r is the reef flat water level. We show that the size of δ determines whether the observed reef flat motions are wave-like or dissipative for the four reefs considered. The linear analytical model provides reasonable predictions of observed low-frequency shoreline significant wave heights given the envelope of the incident free surface elevation, the water level on the reef flat, and the shoaling and breaking parameters derived from the setup analysis.

2. Study Sites

We analyze pressure and current data from four fringing reefs in the western tropical Pacific to motivate the analytic modeling study. Two of the study sites

Table 1. Details of the Sensors Used in This Analysis^a

Sensor		Type	Depth (m)	Position (m)	Record Length (s)	C.S.: B. D. (m)
RC1	(s)	P	0.4	50	5,400	
RC3		P	0.7	200	5,400	
RC4		PUV	0.8	282	5,400	0.1: 0.1
RC5	(f)	P	6.1	410	5,400	
MC2	(s)	P	0.5	44	5,400	
MC3		PUV	0.8	115	5,400	
MC4		P	0.8	152	5,400	
MC6		PUV	1.0	212	5,400	0.1: 0.1
MC7	(f)	P	5.3	280	5,400	
IPG1	(s)	P	0.3	30	7,196	
IPG4		P	0.6	359	7,196	
IPG5		PUV	0.6	396	7,196	
IPG6		P	0.2	416	7,196	
IPG8	(f)	P	8.0	530	7,196	
IPL1	(s)	P	0.5	30	7,200	
IPL2		P	0.5	195	7,200	
IPL4		P	0.7	359	7,200	
IPL8	(f)	P	8.0	530	7,200	
IPN1	(s)	PUV	0.4	30	10,800	
IPN3		PUV	0.3	277	10,800	
IPN5		PUV	0.5	416	10,800	0.2: 0.1 m
IPN8	(f)	PUV	7.9	530	10,800	
SA1	(s)	P	0.4	68	7,196	
SA2	(f)	P	11	280	7,196	

^aSensor: first symbol indicates site (R = ROI, C = CMI, IP = Ipan, SA = Saipan, second indicates deployment, third indicates sensor number (see Figure 1). Sensors used to represent conditions at the shoreline (s), and reef face (f) are indicated; type: P denotes a Sea-Bird SBE26plus and PUV denotes a Nortek Aquadopp, depth: mean sensor depth during deployment; position: ~distance from the shore; record length: duration of 1 Hz sampling for record used; C.S.: B.D.: cell size and blanking distance of the current measurement.

and swell band, H_f (SS, $0.033 < f < 0.35$ Hz for ROI and CMI, and $0.05 < f < 0.2$ Hz for IP and SAI) with the reef flat water level h_r , indicated in color (Figure 2). The wave heights are estimated over the full length of the surface corrected records, and h_r is the average water level of all of the reef flat sensors (Table 1). The maximum H_{ig} for the four sites is 0.61 m for ROI, 0.76 m for CMI, 0.58/0.44/0.58 m for IPG/L/N, respectively, and 0.86 m for SAI. While shoreline IG wave heights are correlated with incident SS wave heights ($r^2 = 0.54$ (ROI), 0.75 (CMI), 0.83 (IPG), 0.71 (IPL), 0.69 (IPN), 0.95 (SAI), all correlations presented have p values less than 0.05, taking into account serial correlation in the time series), considerable scatter exists particularly for ROI and IP. The high correlations seen between H_{ig} and H_f for IPG and SAI are due to the short length of deployment in which only a single large wave event was measured. Some reef flat water level dependence of H_{ig} versus H_f is evident at ROI, IP, and SAI. That observed at IP and SAI is in part due to the water level on the reef flat being setup dominated [Becker et al., 2014].

The evolution of the low-frequency band across the reef for ROI is illustrated in spectrograms of the 5400 s records (Figure 3). All of the spectral estimates presented are convolved with a Hanning window for a ~ 7 degree of freedom estimate. While the 95% confidence intervals associated with this spectral estimate are large (not shown), the estimated spectral peaks are associated with periodicities visible in the time series and are representative of IG variability observed. The top plots show that the low-frequency energy density of the free surface elevation on the reef face (RC5) is most energetic for frequencies > 0.01 Hz and is consistent with a shoaling bound wave [Pequignot et al., 2014]. The spectrogram of the envelope of the reef face free surface elevation, obtained as the magnitude of the analytic signal, shows energy distributed across the low frequency band. On the reef flat moving shoreward, the low-frequency energy presents a banded structure consistent with the excitation of cross-shore modes [Nakaza and Hino, 1991; Pequignot et al., 2009, 2014]. The modes observed in these studies were related to the theoretical open basin modes for a step reef of length L with the spatial structure of the free surface elevation given by

$$\psi_n(x) = \cos(k_n x) \quad 0 < x < L \quad (1)$$

with

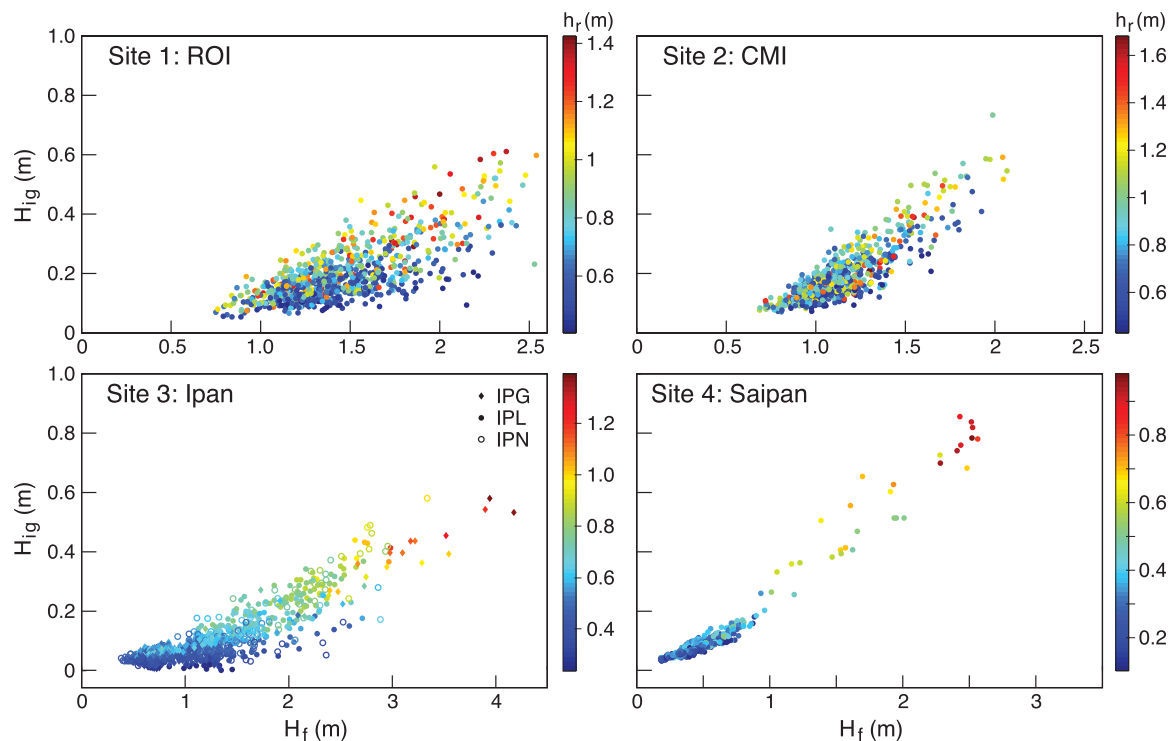


Figure 2. Reef face significant wave heights in the sea and swell band, H_f , versus shoreline significant wave heights in the infra gravity band, H_{ig} , colored with the water level on the reef flat h_r for all sites.

$$k_n = \frac{(2n+1)\pi}{2L} \quad (n=0, 1, 2, \dots) \quad (2)$$

The frequency of the n th mode is

$$\omega_n = \sqrt{gh_r} k_n \quad (3)$$

where h_r is the reef flat water level.

3. IG Observations

We begin with a statistical description of the low frequency variability of the cross-shore pressure and current measurements at ROI, CMI, and IP. During energetic events, the low-frequency variability suggests partially standing, cross-shore modes.

3.1. EOF Analyses and Linear Fluxes

Since the pioneering work of Winant *et al.* [1975], empirical orthogonal function (EOF) analysis has been widely used to assess the dominant variability of dynamical processes in nearshore oceanography. We first carry out EOF analyses at ROI, CMI, and IP to determine the dominant cross-shore spatial and temporal patterns of the low-frequency motion. SAI has only two sensors and is not included in this analysis. For Ipan reef during Tropical storm ManYi (IPG), Pequignet *et al.* [2009] detected cross-shore standing modes on the reef flat using an EOF analysis. Pequignet *et al.* [2014] also noted that cross-shore modes were excited during a large wave event of deployment IPN at Ipan. We note that EOFs, computed as eigenfunctions of the data covariance matrix, are empirical modes. To ascribe physical significance to these modes, we show below that the spatial and temporal behavior of the EOF modes suggest cross-shore modes of an idealized step reef.

For each record, we first bandpass filter the free surface elevation into a frequency band that contains the first two theoretical modes of a step reef for the estimated reef lengths, L , and observed reef flat water

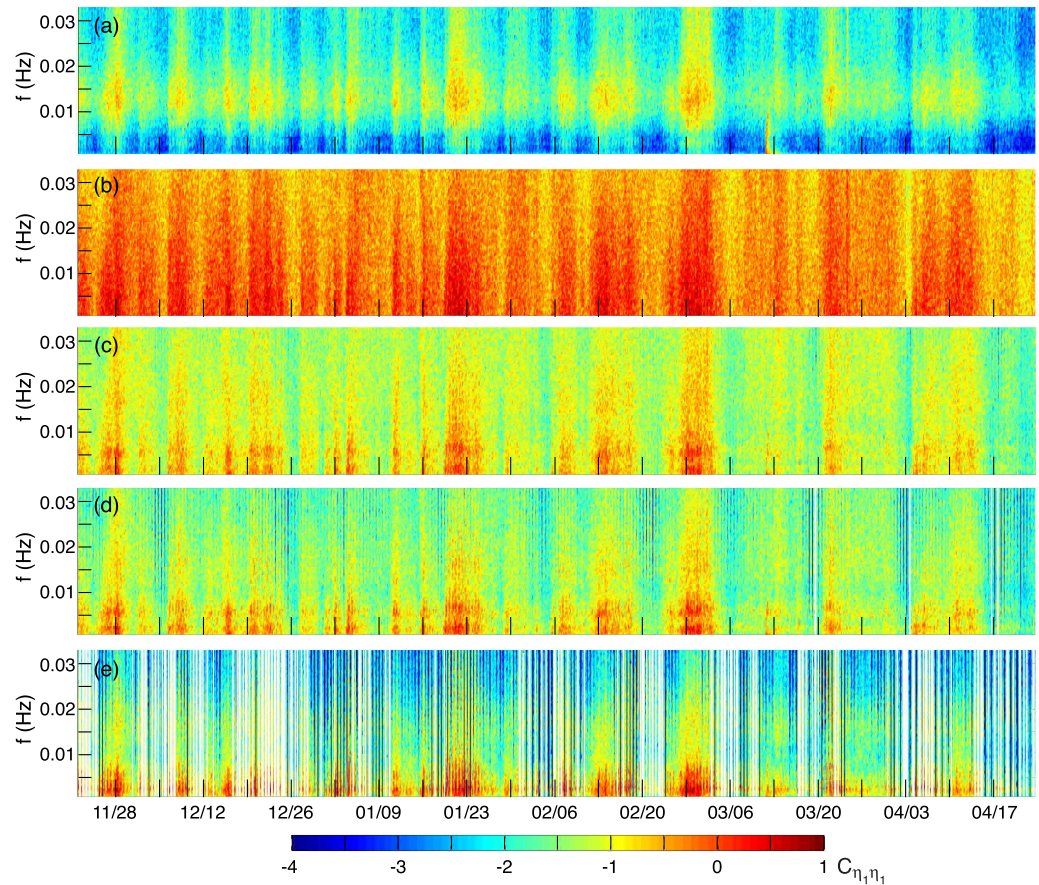


Figure 3. The low-frequency variability across the reef at ROI. The spectrogram (\log_{10}) of (a) the incident free surface elevation at RC5, (b) the envelope of the incident free surface elevation at RC5, and (c)–(e) the reef flat free surface elevation at sensors RC4, RC3, and RC1, respectively. White bands are times when sensors are not submerged.

levels, h_r . We choose this frequency range to minimize contributions from the SS band and bound wave energy (which was shown to work against break point forcing in *Pequignat et al.* [2014]); however, we also quote results from EOF analyses of the entire IG band. The minimum period for theoretical mode 1 is given by $T_1^{\min} = \min(2\pi/\omega_1)$, where ω_1 is defined in (3) with $n=1$. For ROI, $T_1^{\min} \sim 125$ s (achieved for the record with the maximum reef flat water level of $h_r = 1.43$ m), hence we bandpass the free surface elevation to $1/900 < f < 1/100$ Hz. For CMI, with a shorter reef length of $L=220$ m and maximum $h_r = 1.68$ m, $T_1^{\min} \sim 75$ s and we bandpass to $1/900 < f < 1/50$ Hz. For IPL, the widest reef with $L=420$ m and maximum $h_r = 1.20$ m, $T_1^{\min} \sim 165$ s and we use $1/1000 < f < 1/150$ Hz. The band passed free surface elevation $\eta(x, t)$ for the N instrument transect is decomposed into EOFs according to

$$\eta(x, t) = \sum_{j=0}^{N-1} \tilde{\eta}_j^E(x, t) = \sum_{j=0}^{N-1} \tilde{C}_j(t) \tilde{\psi}_j(x). \quad (4)$$

where \tilde{C}_j is the temporal amplitude of the j th EOF spatial mode $\tilde{\psi}_j$.

Representative EOFs for ROI are presented in Figure 4 for three energetic wave events. The wave events have similar incident wave conditions ($H_r = 2.3$ m and T_p between 14 and 16 s), but different water levels on the reef flat. The top plots show the spatial dependence, $\tilde{\psi}_j(x)$, of the first two ($j = 0, 1$) EOF modes, and the bottom plots show spectra of the corresponding temporal amplitudes at the shoreline, $\tilde{\eta}_j^E(x_s, t) = \tilde{C}_j(t) \tilde{\psi}_j(x_s)$, where $x_s = 50$ m for ROI. The first wave event on 21 January 18:00Z, 2011 (Record 486, Figures 4a and 4d) had a relatively high water level on the reef flat ($h_r = 1.24$ m). The first two EOF modes of record 486 describe 95% of the variance in the EOF frequency band (87% in the total IG frequency band), with a spatial dependence resembling the gravest and first theoretical mode of a step reef ((1)–(3),

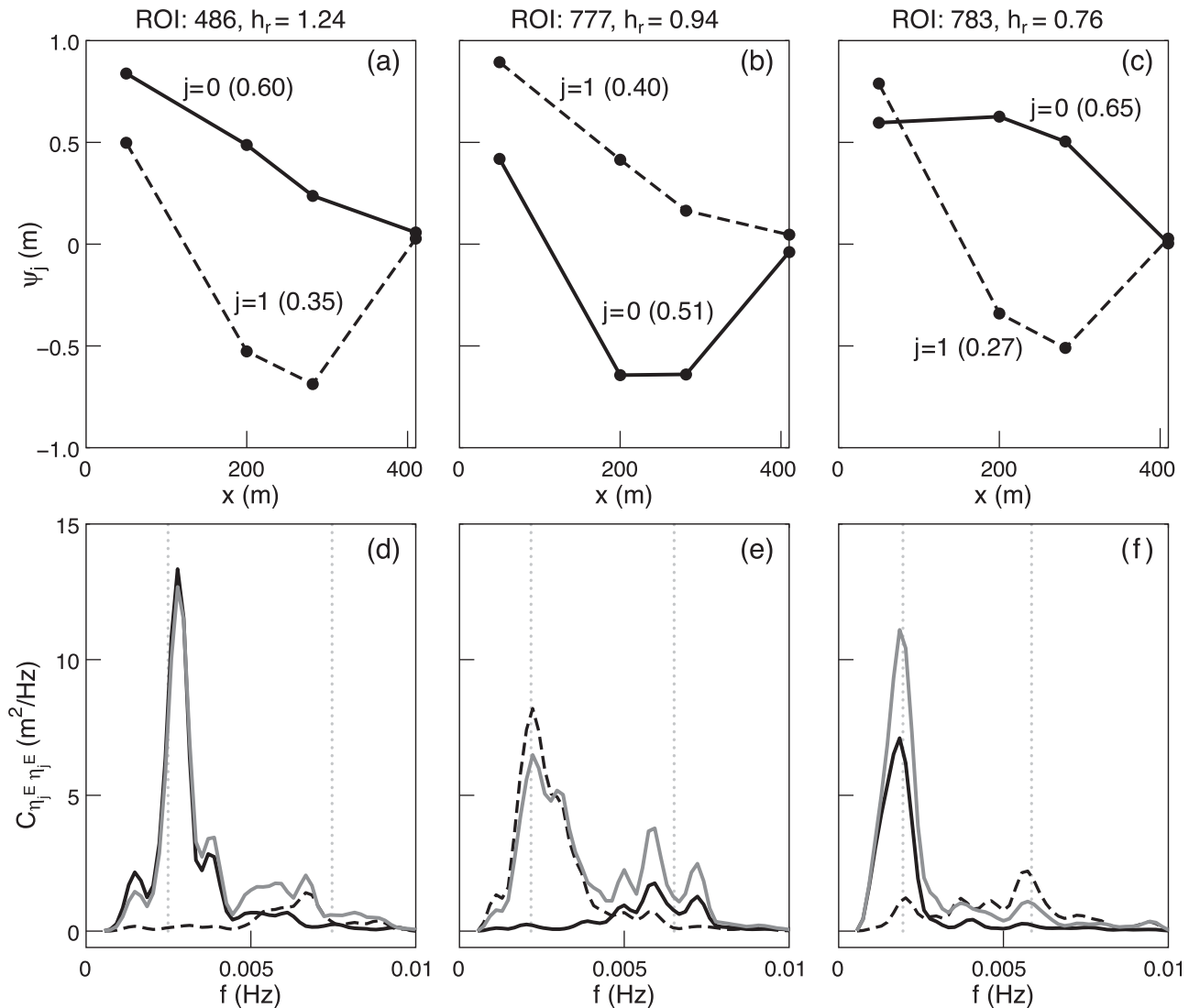


Figure 4. The first two EOFs of the band-passed (100–900 s) free surface elevation for three 1.5 h records at ROI. (a)–(c): Spatial structure across the reef, $\tilde{\psi}_j(x)$, (d)–(f): Spectra of $\tilde{\eta}_j^E(x_s, t)$, from (4). The solid/dashed black line shows the $j=0/1$ EOF, respectively. The vertical-dashed lines denote the theoretical modal frequencies from (3)/ 2π . The variance captured by each EOF mode is indicated in parentheses by the mode number. The grey line on the lower plots is the spectrum of the observed free surface elevation in the EOF band.

$n=0, 1$). In particular, the spatial structure of the first two EOF modes resemble 1/4 and 3/4 wavelength modes, and the spectrum of $\tilde{\eta}_0^E(x_s, t)$ shows a dominant peak near the theoretical (for a step reef) mode $n=0$ frequency, and a smaller peak near the theoretical mode $n=1$ frequency for the spectrum of $\tilde{\eta}_1^E(x_s, t)$.

The EOFs of the second wave event of 27 February 03:00Z, 2011 (Record 777), with a moderate reef flat water level ($h_r=0.94$ m), also suggest the excitation of the gravest and first mode of a step reef, however, the modes have switched order. This is due to significantly less energy near the theoretical mode $n=0$ frequency in the envelope of the reef face forcing for record 777 compared to records 486 and 783 (see section 4.3). The mode $j=0$ EOF explaining 51%/48% of the variance in the EOF/IG band has one zero crossing consistent with a 3/4 wavelength ($n=1$) theoretical mode on the reef flat and high-frequency energy (Figures 4b and 4e); the mode $j=1$ EOF describing an additional 40%/39% of the variance in the EOF/IG band has no zero crossing consistent with a 1/4 wavelength ($n=0$) theoretical mode on the reef flat and low-frequency energy (Figures 4b and 4e). The spectrum of $\tilde{\eta}_j^E(x_s, t)$ ($j=0, 1$, Figure 4e) shows significantly more elevation energy at the shoreline in the gravest mode ($n=0$, EOF $j=1$) than the first mode even though the first mode ($n=1$, EOF $j=0$) accounts for more variance across the reef flat (sensor RC1 is located near the node of the $n=1$ theoretical mode). The third event of 27 February 21:00Z, 2011 (Record

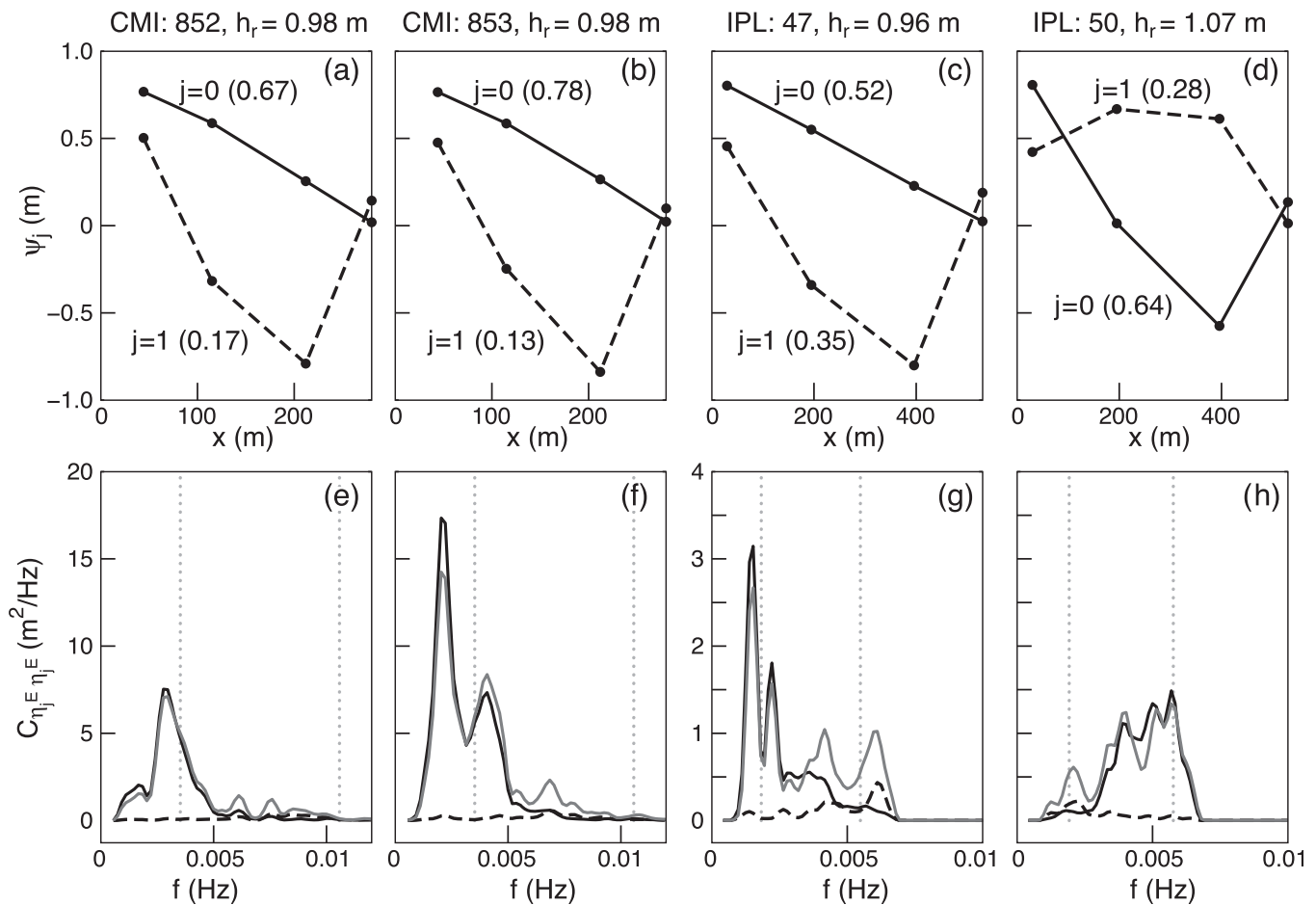


Figure 5. The spatial structure, $\bar{\psi}_j$ and spectra of $\bar{\eta}_j^E(x_s, t)$ of the first two EOF modes for CMI (sensors MC7, MC4, MC3, and MC2) and IPL. (a), (b), (e), (f) EOFs of the band passed (50–900 s) free surface elevation for two 1.5 h records at CMI. (c), (d), (g), (h), EOFs of the band passed (150–1000 s) free surface elevation for 2 h records at IPL. The solid/dashed black line shows the $j=0/1$ EOF, respectively. Note the difference in vertical scale for CMI and IPL for the spectra. The vertical-dashed lines denote the theoretical modal frequencies from $(3)/2\pi$. The variance captured by each EOF mode is indicated in parentheses by the mode number. The grey line on the lower plots is the spectrum of the observed free surface elevation in the EOF band.

783) demonstrates the effect of low reef flat water level ($h_r = 0.76$ m) on an energetic wave event for ROI (Figures 4c and 4f). The EOF mode $j = 0$ (65%/62% of the variance in the EOF/IG band) suggests the excitation of the gravest ($n=0$) cross-shore mode similar to the first event shown in Figures 4a and 4d. The lower water level of the third event results in a lower peak frequency in the spectrum of the time amplitude of EOF mode $j = 0$ than for the first event (Figures 4d and 4f), consistent with the water level dependence in (3). In addition, comparing the EOF mode $j = 0$ spatial structure of Figures 4a and 4c, we find that the amplitude slightly decreases shoreward between sensors RC3 and RC1 for the lower water level record. The observed values of H_{ig} nearest the shoreline for the three events are 0.60, 0.57, and 0.52 m, respectively.

For CMI, the EOF analysis reveals how water level may impact the generation of extreme amplitude IG energy at the shoreline (Figures 5a, 5b, 5e, and 5f). A wave event over a 6 h period with $H_r = 2$ m, and $T_p = 14$ –16 s occurred at peak tide ($h_r = 0.98$ m). Over the first 3 h period (sampled for 5400 s) a strong modal response was observed on the reef flat (Figures 5a and 5e, 27 February 12:00Z, 2011, record 852) leading to a shoreline 5400 s IG wave height of $H_{ig} = 0.54$ m. The subsequent 3 h period (27 February 15:00, 2011, record 853, sampled for 5400 s) had the largest observed IG shoreline wave height of the deployment, $H_{ig} = 0.76$ m. The near constant water level over the 6 h period led to enhanced excitation of the EOF $j = 0$ mode by the wave event (Figures 5b and 5f).

IP has a longer reef flat with smaller tidal range than ROI and CMI. For IPL, we present EOFs from two wave events (10 December 20:00Z, 2008, $H_r = 2.7$ m and 11 December 08:00Z, 2008, $H_r = 3.0$ m, records 47 and

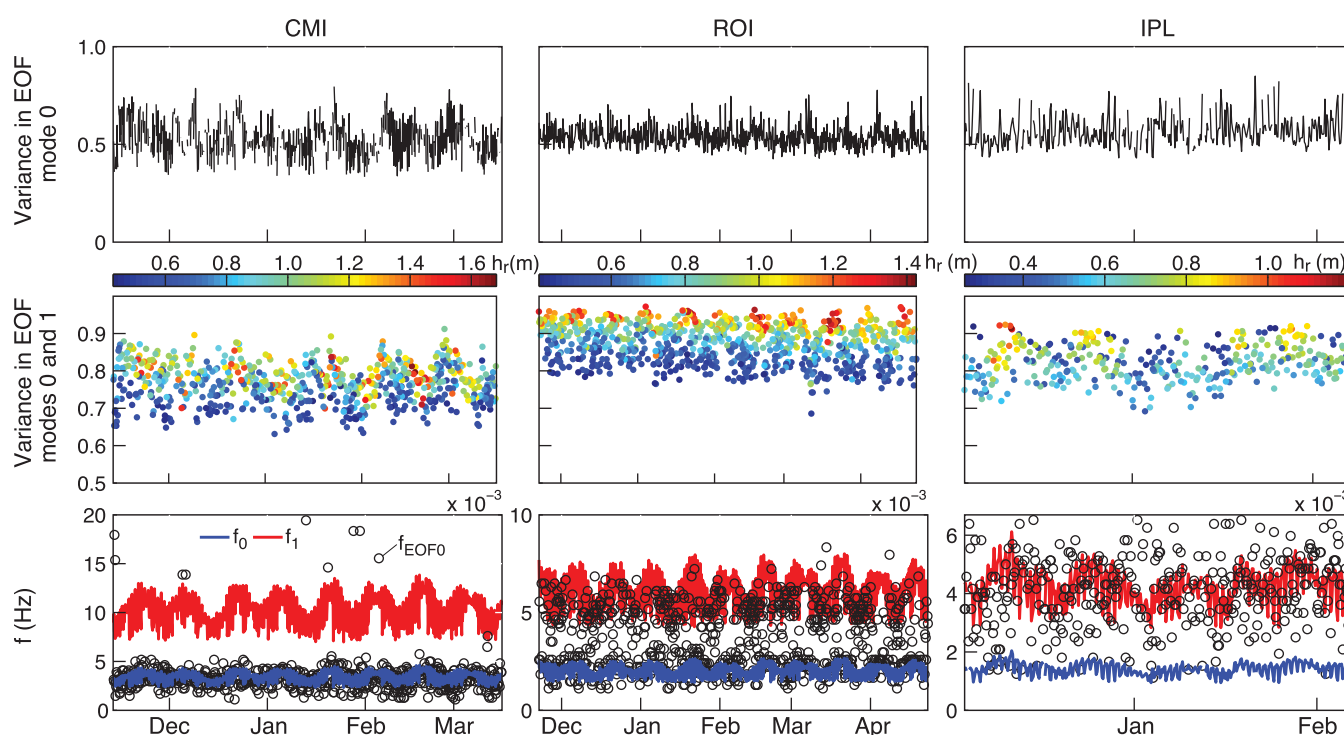


Figure 6. EOF variance and modal selection for CMI, ROI, and IPL (left to right plots, ordered by increasing reef length) for the band-passed free surface elevation. (top) Time series of the variance in EOF mode $j = 0$ over the deployment. (middle) Time series of the variance in EOF modes $j = 0$ and $j = 1$ colored by water level on the reef flat. (bottom) Time series of the gravest (blue) and first (red) theoretical modal frequency with the peak frequency of EOF 0 superimposed (black circles).

50) with similar reef flat water levels ($h_r = 0.96$ and 1.07 m, respectively) and incident peak periods ($T_p = 13$ s). For the first/second event, the dominant ($j = 0$) EOF mode is consistent with the excitation of the gravest ($n = 0$)/first ($n = 1$) mode of a step reef as the envelope of the reef face forcing for the second event near the theoretical $n = 0$ frequency is significantly less energetic than for the first event (see section 4.3). While cross-shore modes appear to be excited on the reef flat (Figures 5c and 5d), the amplitudes are significantly less energetic than observed at ROI and CMI (Figures 5g and 5h). In addition for the second event (Figure 5d, record 50), the EOF mode $j = 1$ (similar to the gravest theoretical mode, $n = 0$) shows decay shoreward suggesting the importance of dissipation. The values of the observed shoreline H_{ig} for these two events are 0.38 and 0.37 m, respectively.

The deployment-averaged percentage of the variance in the EOF/IG band described by the $j = 0$ EOF mode is 54/44%, 52/49%, and 57/40%, for ROI, CMI, and IPL which is consistent with the variable bandwidths chosen for the EOF analysis (i.e., the EOF band is 92, 98, and 87% of the IG band for ROI, CMI, and IPL, respectively). The first two ($j = 0, 1$) EOF modes describe 87/72%, 76/72%, and 82/59% of the variance in the EOF/IG band. The top plots of Figure 6 present time series of the variance described by the mode $j = 0$ EOF in the EOF band for ROI, CMI, and IPL. The middle plots present a scatter plot of the variance described by the first two EOF modes $j = 0$ and $j = 1$ in the EOF band for each of the sites colored by reef flat water level h_r . The EOFs describe a larger percentage of the variance for higher reef flat water levels, which is particularly evident at ROI. As discussed below in section 5, the reef response is more modal and less dissipative at high water levels.

The effect of reef length on the dominant ($j = 0$) mode selected by the EOF analysis is illustrated in the bottom plots of Figure 6. The solid blue and red traces are the first two theoretical modal frequencies, f_0 and f_1 from (3) (divided by 2π), for each site. Superimposed on the theoretical modal frequencies is the peak frequency of the estimated spectrum of the time amplitude of EOF mode $j = 0$. For the shorter reef of CMI ($L \sim 220$ m), the peak frequency of the time amplitude of EOF $j = 0$ is dominantly the theoretical mode $n = 0$ (Figures 5a, 5b, 5e, and 5f). For the intermediate reef length of ROI ($L \sim 350$ m), the peak frequency of the time amplitude of the dominant EOF mode is either theoretical mode $n = 0$ or mode $n = 1$, consistent

with the results of Figure 4 (i.e., records 486 versus 777). For the longest reef, IPL ($L \sim 420$ m), the peak frequency of the time amplitude of the dominant EOF mode shows significant scatter predominantly around the theoretical mode $n = 1$ frequencies (Figures 5c, 5d, 5g, and 5h).

The EOF analysis suggests that the majority of the variability in the IG band is consistent with the excitation of cross-shore modes, particularly at high water levels. To assess the degree to which these modes are standing, we next estimate the incoming and outgoing linear energy flux shoreward of the reef crest using the pressure and current measurements at the PUVs for ROI, CMI, and IPN (RC4, MC6, and IPN5). We first determine the principle axes of the total energy flux ($f_1 = 1/900$ Hz, $f_2 = 0.35$ Hz for ROI and CMI and $f_1 = 0.001$ Hz, $f_2 = 0.2$ Hz for IPN) defined as

$$[F_{ew}, F_{ns}] = gh \int_{f_1}^{f_2} [\text{Co}(\eta, u_{ew}), \text{Co}(\eta, v_{ns})] df \quad (5)$$

where (u_{ew}, v_{ns}) are the east-west and north-south current components, h is the water level at the PUV, and Co is the cospectrum. We rotate the currents into these principle axes to obtain the cross-shore and along-shore currents (u_r, v_r) and estimate the cross-shore incoming and outgoing linear energy flux from *Shere-met et al.* [2002]

$$\mathcal{F}^{\pm}(f) = \frac{\sqrt{g^3 h}}{4} [\text{Co}_{\eta, \eta}(f) + (h/g) \text{Co}_{u_r, u_r}(f) \pm 2\sqrt{h/g} \text{Co}_{\eta, u_r}(f)]. \quad (6)$$

Figure 7 presents the band-integrated incoming and outgoing cross-shore energy flux, F^{\pm} , for the EOF frequency band (top plots) and the IG frequency band (bottom plots) for RC4, MC6, and IPN5 colored with the water level at each PUV. For all sites, the band-averaged outgoing flux increases with both incoming flux and water level. For the shorter reefs at CMI ($L \sim 220$ m) and ROI ($L \sim 350$ m), the incoming and outgoing linear energy flux in the EOF bands are comparable suggesting partially standing modes. The records used in the EOF analyses of Figures 4 and 5a, 5b, 5e, and 5f) are indicated in Figure 7.

3.2. Cross-Covariance: Break-Point Forcing

Break point forcing has been shown to be a mechanism to generate IG waves on sandy beaches [Symonds et al., 1982]. For steep reefs, break point forcing has been observed in field studies [Pomeroy et al., 2012; Pequignet et al., 2014], and in laboratory and numerical studies [e.g., Baldock, 2006; Su et al., 2015]. While we do not have direct observations of breaking, we here perform a cross-covariance analysis following Pomeroy et al. [2012] between the envelope of the incident free surface elevation and the IG free surface elevation across the reef for ROI (Figure 8). A positive covariance between the envelope of the incident waves and the reef flat response is indicative of breakpoint forcing, whereas a negative covariance typically occurs for forced difference interactions [Pomeroy et al., 2012].

We first consider the cross covariance for two consecutive elevation wave records (28 November 06:09:00Z, 2010) during falling tide (top plot, 8). The cross covariance between the envelope of the reef face free surface elevation and the reef face IG free surface elevation (i.e., prior to breaking) is large and negative, consistent with a shoaling bound wave on the reef face. The cross covariance between the envelope of the reef face free surface elevation and the IG free surface elevation on the reef flat (after breaking) is large and positive with increasing lag and decreasing amplitude moving shoreward across the reef flat. As the falling tide reduces the reef flat water level, the lag at maximum cross covariance increases for the second record consistent with the water level dependence of the long wave phase speed. The bottom plot of Figure 8 presents the maximum cross-covariance across the reef for ROI for records with $H_{ig} > 0.30$ m, colored with water level on the reef flat, and confirms the results of the top plot over the deployment. The cross covariance before breaking between the incident envelope and free surface elevation is strongly negative, and that between the incident envelope and the reef flat response after breaking is consistently positive, with lag increasing with decreasing water level. Cross-covariance analyses of observations at CMI and IP over steep reef faces also are consistent with break point forcing.

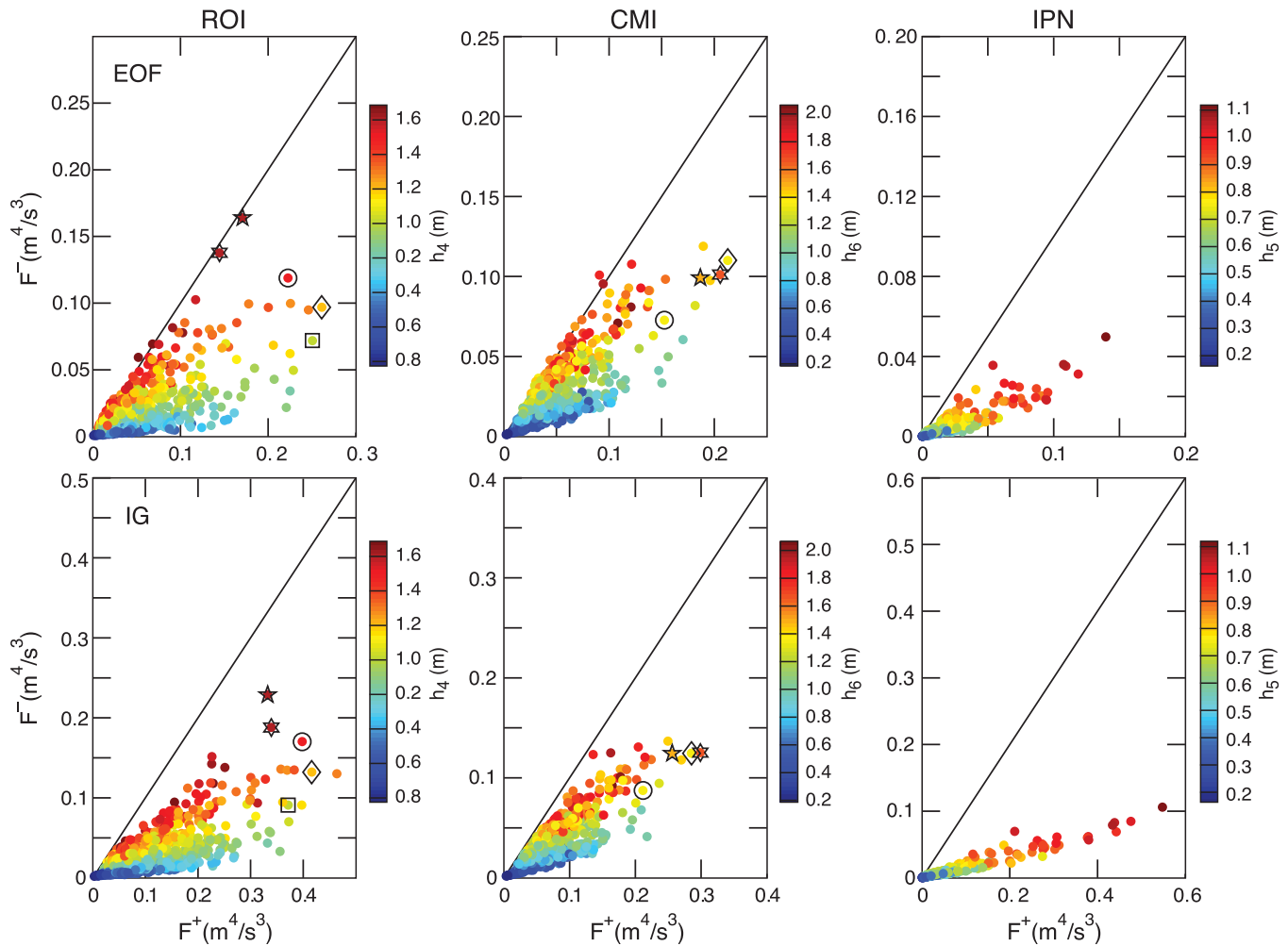


Figure 7. The linear incoming and outgoing energy flux at sensors colored with the water level at RC4 (a, d), MC6 (b, e), and IPN6 (c, f) from (6) averaged over the EOF band (top), and the IG band (bottom). In Figures 7a and 7d, the circle, triangle, and square denote records 486, 777, and 783 (Figures 4 and 10) and the penta and hexa star denote records 481 and 482, respectively (Figure 11). In Figures 7b and 7e, the circle and triangle denote records 852 and 853 (Figure 5), and the penta and hexa star denote records 864 and 865, respectively (Figure 11).

4. Linear Model

The statistical analyses of the observations presented in section 3 suggest that the low-frequency variability consists of partially standing, cross-shore modes with properties similar to modes of a theoretical step reef. For steep reefs such as those studied here, break-point forcing has been shown to generate low-frequency motions. We derive in the Appendix A a linear analytical model that follows from an extension of the point break model of setup [Vetter *et al.*, 2010; Becker *et al.*, 2014] that governs IG motions on the reef flat. This model, first applied in Merrifield *et al.* [2014], is evaluated here against the observations as a linear input-output system. The linear analytical model predictions, that rely on empirical parameters from the setup analyses, also are compared with observations with reasonable agreement.

4.1. Transfer Function

Equation (4) in Merrifield *et al.* [2014] is

$$\frac{\partial^2 \bar{\eta}_n^{(c)}}{\partial t^2} + \mathcal{D} \frac{\partial \bar{\eta}_n^{(c)}}{\partial t} + \omega_n^2 \bar{\eta}_n^{(c)} = (-1)^n \frac{3}{32} g \gamma_b k_n h_r H_b(t). \quad (7)$$

where $\bar{\eta}_n^{(c)}$ is the Fourier cosine transform of $\eta(x, t)$ (A5). It is straightforward to solve (7) in the frequency domain with

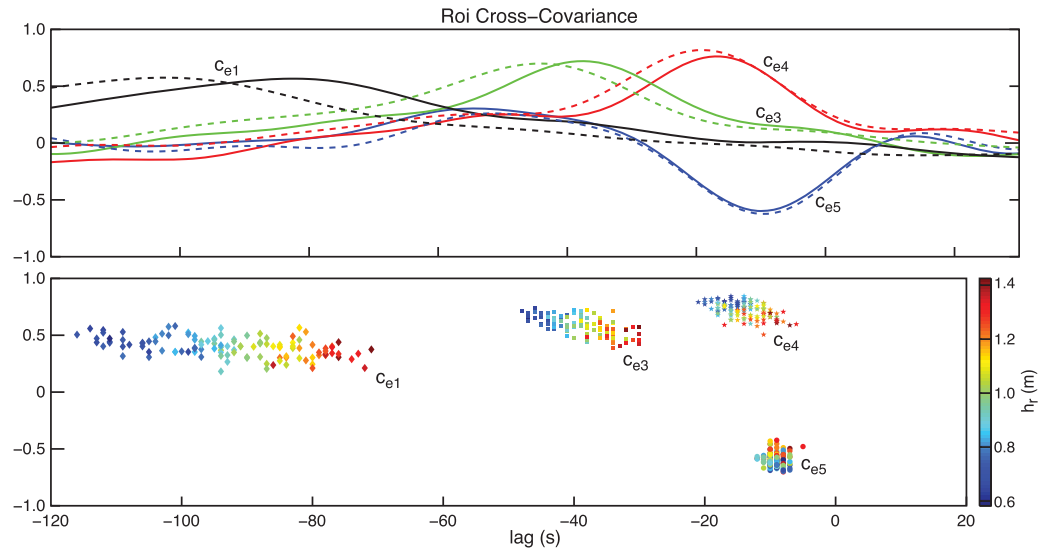


Figure 8. Breakpoint forcing: Cross-covariance as a function of spatial lag between the envelope of the SS free surface elevation at RC5 and the free surface elevation (c_{ei}) at RC5, RC4, RC3, and RC1 for (top) two consecutive 1.5 h records at falling tide and (bottom) for all records at ROI with $H_{lg} > 0.3$ m colored with water level on the reef flat. (top) The solid and dashed lines were derived from 28 November 09:00Z, 2010 (Record 51), and 28 November 09:00Z, 2010 (Record 52).

$$\bar{\eta}_n^{(c)} = \hat{\eta}_n^{(c)} e^{i\omega t}, \quad H_b = \hat{H}_b e^{i\omega t}. \quad (8)$$

where $\hat{\eta}_n^{(c)} \equiv \hat{\eta}^{(c)}(k_n, \omega)$. We find

$$\hat{\eta}_n^{(c)} = \mathcal{A}_n(\omega) \hat{H}_b, \quad \mathcal{A}_n(\omega) = A_n(\omega) e^{-i\phi_n(\omega)} \quad (9)$$

where $\mathcal{A}_n(\omega) \equiv \mathcal{A}(k_n, \omega)$ (and similarly for $A_n(\omega)$, $\phi_n(\omega)$),

$$A_n(\omega) = \frac{3g\gamma_b k_n h_r / 32}{\sqrt{(\omega_n^2 - \omega^2)^2 + (\mathcal{D}\omega)^2}} \quad (10)$$

and

$$\phi_n(\omega) = \tan^{-1} \left[\frac{(-1)^n \mathcal{D}\omega}{(-1)^n (\omega_n^2 - \omega^2)} \right]. \quad (11)$$

Inverting the Fourier cosine transform, and invoking (9), we obtain

$$\hat{\eta}(x, \omega) = \sum_{n=0}^{\infty} \hat{\eta}_n(x, \omega) = \sum_{n=0}^{\infty} \mathcal{T}_n(x, \omega) \hat{H}_b(\omega), \quad (12)$$

$$\mathcal{T}_n(x, \omega) = \frac{2}{L} \mathcal{A}_n \cos k_n x \equiv G_n(x, \omega) e^{i\Phi_n(x, \omega)} \quad (13)$$

where $\mathcal{T}_n(x, \omega)$ is the modal transfer function for the linear input, $\hat{H}_b(\omega)$, output, $\hat{\eta}(x, \omega)$, system described by (7) and (8). In (13), $G_n(x, \omega)$ and $\Phi_n(x, \omega)$ are the gain and phase of the modal transfer function. In section 4.2, we compare the theoretical transfer function (13) with that obtained from a cross-spectral analysis of the observations with the breaking wave height taken as the shoaled envelope of the reef face free surface elevation.

We also solve (7) with a Fourier transform in time (i.e., $\hat{\eta} = \mathcal{F}[\eta]$) yielding the theoretical approximation to the reef flat free surface elevation used in Merrifield *et al.* [2014] (note that a factor of 1/2 is missing from their Equation (7) since their $\mathcal{B}_n = \frac{2}{L} \mathcal{A}_n$)

$$\eta(x, t) = \sum_{n=0}^{\infty} \mathcal{F}^{-1}[\hat{\eta}_n(x, \omega)] \quad (14)$$

where \mathcal{F} and \mathcal{F}^{-1} are the forward and inverse temporal Fourier transforms, respectively. We compare (14) with the observed values of the IG shoreline wave heights in section 4.3.

Table 2. Parameters Used in the Estimates of the Theoretical Transfer Functions (13), the Breaking Wave Height, $\tilde{H}_b(t)$, (16), and the Predicted Reef Flat Free Surface Elevation, $\tilde{\eta}(x, t)$, (18)^a

Site	L (m)	γ_b	s_b	\mathcal{D}
ROI	350	$1.2 - 0.5h' + 0.2h'^2$	1.3	0.004
CMI	220	$1.1 - 0.2h'$	1.3	0.006
IP	420	$1.3 - 0.4h'$	1.3	0.008
SAI	135	$1.4 - 0.7h'$	1.4	0.011

^a h' is a proxy of the tide taken as the detrended water level at the reef face sensor for each site.

4.2. Spectral Transfer Functions

For a linear input-output system, the spectral transfer function is defined as

$$\tilde{T}(x, f) = \frac{S_{XY}(x, f)}{C_{XX}(x, f)} \quad (15)$$

where S_{XY} is the cross spectrum between the input, $X(x, t)$, and the output, $Y(x, t)$, C_{XX} is the input auto spectrum at the position x , and $f = \omega/2\pi$. We perform a cross spectral analysis using the observations

described in Table 1. The input time series of the significant breaking wave height, $X = \tilde{H}_b$, is estimated as $2\sqrt{2}$ times the low-pass filtered envelope of the sea and swell band free surface elevation at the reef face sensor, η_f , shoaled to breaking hence

$$\tilde{H}_b(t) = 2\sqrt{2}s_b|\eta_f + iHil[\eta_f]| \quad (16)$$

and Hil is the Hilbert transform. The shoaling is carried out simply by multiplying the envelope by a factor consistent with a comparison of the estimated 15 min average breaking wave heights versus reef face wave heights using the method in Becker *et al.* [2014]. For all sites the shoaling factor is $s_b \sim 1.3-1.4$ (Table 2). The output time series is the free surface elevation at location x on the reef flat. We define the gain and phase of the estimated transfer function as

$$\tilde{T}(x, f) = \tilde{G}_{XY}(x, f)e^{-i\tilde{\Phi}_{XY}} \quad (17)$$

We estimate the transfer function from the observations using (17) with input $X = \tilde{H}_b(t)$ from (16), and the free surface elevation at the sensor closest to the shoreline, $Y = \eta_i$, as the output, η_i (i = sensor number). Figure 9 presents spectrograms of \tilde{H}_b , $C_{\tilde{H}_b\tilde{H}_b}$, (top plots) the gain $\tilde{G}_{\tilde{H}_b\eta_i}$ (middle plots) and phase, $\tilde{\Phi}_{\tilde{H}_b\eta_i}$ (bottom plots) of the transfer function (17) for an extended energetic wave event at ROI (26 February 06:00Z to 28 February 18:00Z, 2011) and CMI (26 February 15:00Z to 1 March 03:00Z, 2011). The energy of the breaking wave height spectra (Figure 9 top) spans most of the IG band and differs from the spectra of the envelope of the free surface elevation presented in Figure 3b only by the scaling factor $2\sqrt{2}s_b$ (note the different

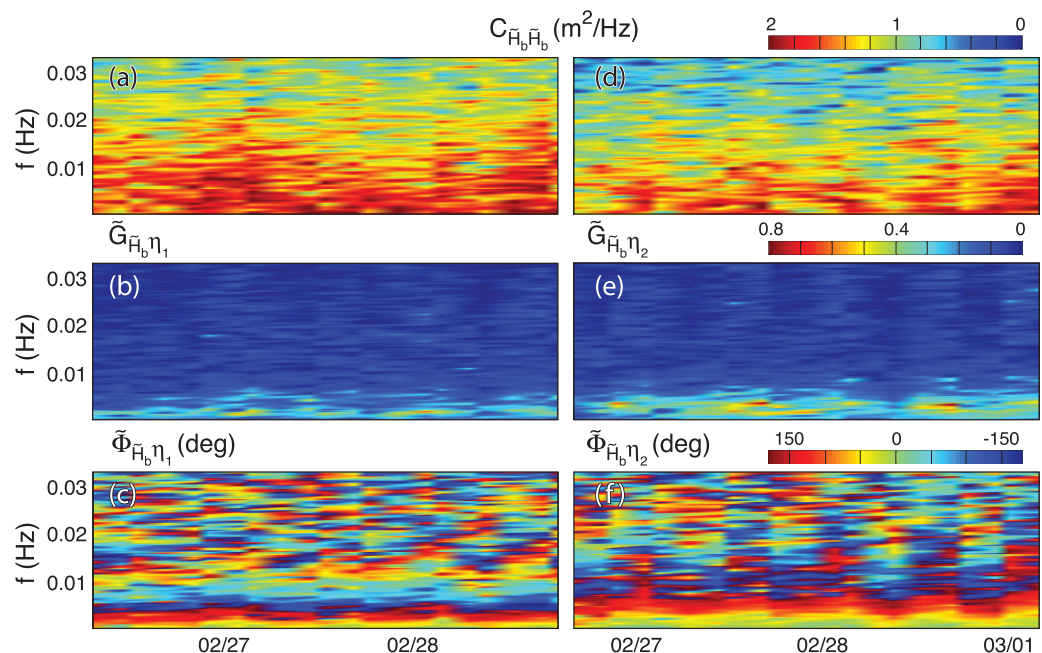


Figure 9. Linear transfer functions during an energetic wave event at ROI (a)–(c) and CMI (d)–(f). (top) Spectrum of the input breaking wave height, $C_{\tilde{H}_b\tilde{H}_b}$. (middle and bottom) Gain and phase of the observed transfer function, $\tilde{G}_{\tilde{H}_b\eta_i}$ and $\tilde{\Phi}_{\tilde{H}_b\eta_i}$ from (17).

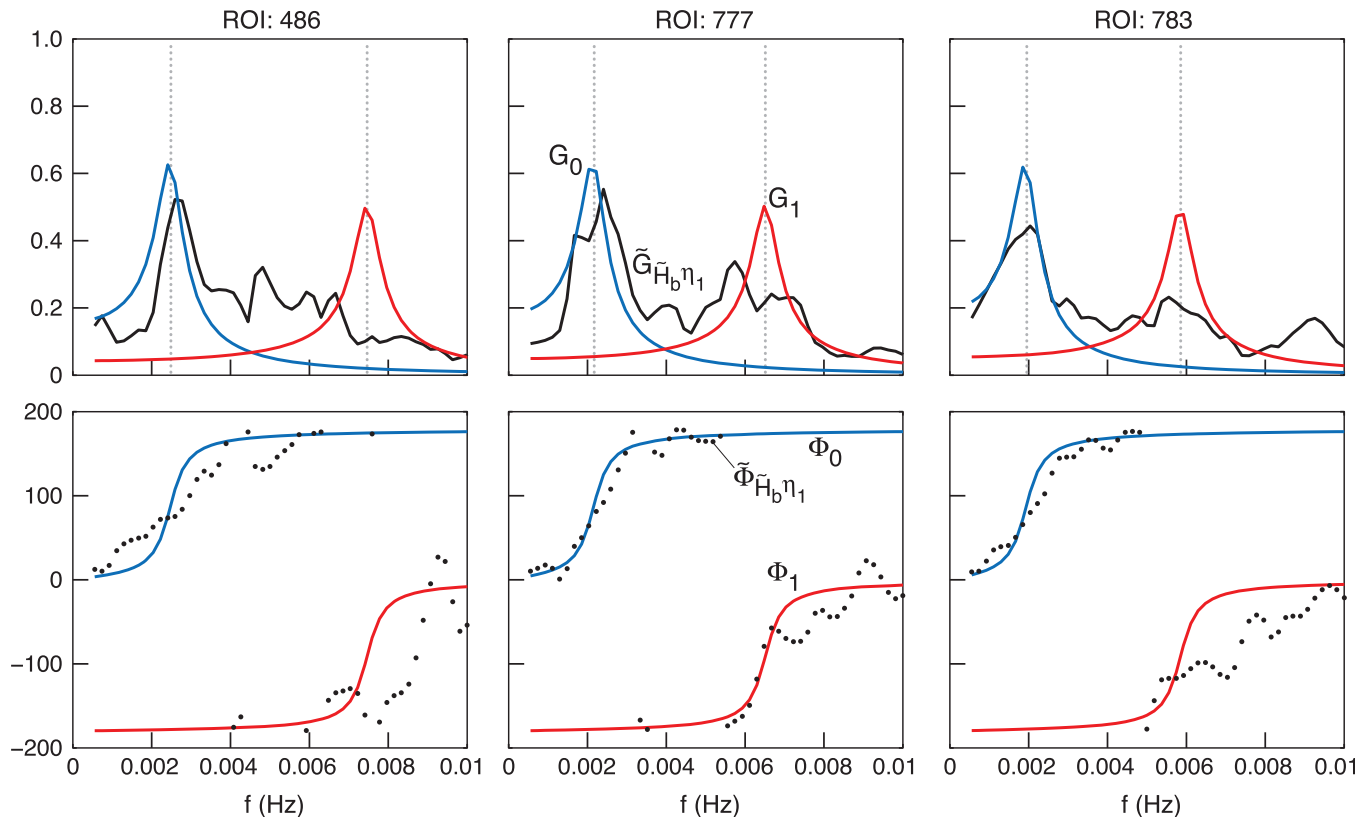


Figure 10. The modal transfer functions, (13), for the parameters of Table 2 and the observed transfer functions, (17), for the records of Figure 4. (top) modal gain, G_0 (blue), G_1 (red), and observed gain $\tilde{G}_{\tilde{H}_b \eta_1}$ (black), and (bottom) modal phase, Φ_0 (blue), Φ_1 (red), and observed phase $\tilde{\Phi}_{\tilde{H}_b \eta_1}$ (black dots). The vertical grey-dotted lines denote the first two modal frequencies from (3)/2 π .

color bar scales). The frequency dependence of the gain of the transfer function (Figure 9, middle) clearly shows that the reef acts as a low pass filter consistent with the spectra of the observed free surface elevation across the reef (Figures 3c, 3d, and 3e). The phase of the transfer function (Figure 9, bottom) presents a banded structure in the frequency range where the gain of the transfer function is amplified.

We next compare the transfer function (17) estimated from the observations, with the transfer function from the linear analytical model derived in section 4.1. We compute the modal transfer function, (13), using the water level on the reef flat, h_r , the reef length L and the modal wavenumber and frequency from (2) and (3). We take γ_b from the setup analysis of Becker *et al.* [2014]; hence, the only adjustable parameter in (13) is the dissipation \mathcal{D} . The empirical values of s_b and γ_b used here are provided in Table 2 for the four sites. In Figure 10, we present the theoretical (13) and observed (17) transfer functions for the three records from ROI of Figure 4. Qualitative agreement is obtained between the theoretical and observed gain (top plots) and phase (bottom plots) of the transfer functions for $\mathcal{D} = 0.004$. In particular, the gain of the transfer function estimated from the observations is amplified near the peak in the $n=0$ analytical transfer function. The phase of the observed transfer function also is in qualitative agreement with the analytical phase in the frequency ranges where modes $n=0, 1$ are energetic. The banded phase structure of Figure 9 is apparent in the theoretical and observed phase estimates of Figure 10 (bottom plots). We remark that the value of $\mathcal{D}=0.005$ in (13) used in Merrifield *et al.* [2014] also provides a modal transfer function that is consistent with the estimated transfer functions presented in Figure 10. We use $\mathcal{D} = 0.004$ due to the use of slightly different values of γ_b used here (see correction to Becker *et al.* [2014]).

4.3. Forcing Characteristics and Tidal Phase

The linear analytical model suggests that the spectral characteristics of the forcing, \tilde{H}_b , and tidal phase affect the IG motions on the reef flat. We next present observational evidence of how the envelope forcing and tidal phase affect the IG shoreline response. Figure 11 shows the input, $C_{\tilde{H}_b \tilde{H}_b}$, and output, $C_{\eta_1 \eta_1}$, spectra

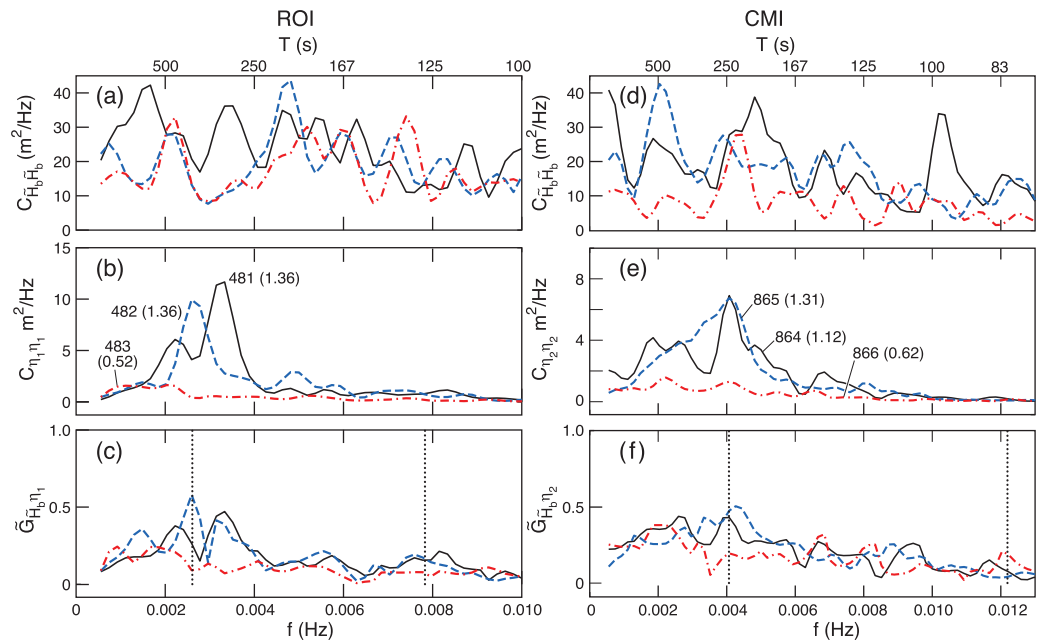


Figure 11. Effects of forcing characteristics and tidal phase on the shoreline response for three consecutive 1.5 h events at ROI, (a)–(c) and CMI, (d)–(f). (top) Input spectra, $C_{\tilde{H}_b \tilde{H}_b}$, (middle) Output spectra, $C_{\eta_i \eta_i}$ ($i = 1, 2$ for ROI and CMI, respectively), and (bottom) Gain of the transfer function, $\tilde{G}_{\tilde{H}_b \eta_i}$ from (17). The vertical-dotted grey lines denote the first two theoretical modal frequencies from $(3)/2\pi$ for records 482 and 865, respectively.

of three consecutive records over a 9 h period from ROI (21 January 03:00–09:00Z 2011, records 481, 482, and 483) and 2 (10 March 0:00–06:00Z, 2011, records 864, 865, and 866) for energetic wave events that occurred during peak tide.

The effects of the evolving forcing on the shoreline response for ROI are shown in the left plots of Figure 11. The incident reef face wave height, H_f , peak period T_p , and reef flat water level, h_r are 2.4, 2.2, and 2.1 m, 16, 16, and 14 s, and 1.36, 1.36, and 0.52 m for the three records, respectively. For record 481 for ROI, the two lowest frequency peaks in the spectrum of the breaking wave height $C_{\tilde{H}_b \tilde{H}_b}$ occur near periods of ~ 600 and 300 s, respectively (Figure 11a). The spectral response of the shoreline free surface elevation at sensor RC1, $C_{\eta_1 \eta_1}$, for record 481 follows the peak in the forcing near the frequency of the gravest normal mode and exhibits a peak near ~ 300 s (Figure 11b). The theoretical modal period for record 481 is $T_0 \sim 385$ s estimated from (3) for the observed water level $h_r = 1.36$ m. The gain of the estimated transfer function for record 481 shows spectral peaks near the peaks of the shoreline response, $C_{\eta_1 \eta_1}$ (Figures 11b and 11c). Records 481 and 482 occur at peak tide and have the same $h_r = 1.36$ m since the water level on the reef flat at ROI is tidally dominated [Becker et al., 2014]. The input spectrum $C_{\tilde{H}_b \tilde{H}_b}$ for record 482 has evolved to exhibit low-frequency peaks near periods of ~ 210 and 450 s, respectively (Figure 11a). The shoreline spectrum for record 482 shows a peak near the theoretical modal period of $T_0 \sim 385$ s as does the gain of the transfer function (Figures 11b and 11c). The near constant water level at peak tide for records 481 and 482 and the energetic envelope at low frequencies has resulted in the excitation of a cross-shore mode similar to the gravest normal mode. Figure 7a also supports a modal interpretation as records 481 and 482 have nearly equal incoming and outgoing linear energy flux in the EOF band ($1/900 < f < 1/100$ Hz). The third record in this sequence, 483, occurs at falling tide, and while the spectrum of \tilde{H}_b , $C_{\tilde{H}_b \tilde{H}_b}$, is slightly less energetic than for the previous records, the shoreline response is reduced significantly. The IG wave heights at the shoreline, H_{ig} are 0.61, 0.58, and 0.28 m for records 481, 482, and 483, respectively.

The effects of the forcing characteristics and tidal phase also are evident in the CMI IG shoreline response (right plots of Figure 11). For CMI, the incident reef face wave height, H_f , peak period T_p , and reef flat water level, h_r are 2.0, 2.0, and 1.7 m, 14, 15, and 14 s, and 1.12, 1.30, and 0.62 m for the three records, respectively. Here, record 864 shows a shoreline response, $C_{\eta_2 \eta_2}$ (Figure 11e), that follows the frequency content of the forcing, $C_{\tilde{H}_b \tilde{H}_b}$ (Figure 11d), with a dominant peak period near ~ 250 s close to the theoretical modal period

of $T_0 \sim 270$ s ($h_r = 1.12$ m). The low-frequency spectral content of the forcing $C_{\tilde{H}_b \tilde{H}_b}$ (Figure 11d) for subsequent record 865 shows an energetic spectral peak near ~ 500 s while the shoreline response, $C_{\eta_2 \eta_2}$ (Figure 11e), shows a broader spectral peak near ~ 250 s, the theoretical modal period for record 865 for the gravest mode. The gain of the transfer function for record 865 also is peaked near this theoretical modal period (Figure 11f). Again, as the tide falls and the incident forcing is less energetic (record 866), the shoreline response is significantly reduced. The IG wave heights at the shoreline, H_{ig} , are 0.58, 0.59, and 0.31 m for records 864, 865, and 866, respectively.

The above results indicate that the reef flat response may follow the forcing due to breaking at the time scale of the envelope. When reef flat water levels hold constant due to peak tidal phase for tidally dominated reef flat water levels, or large setup for setup dominated reef flat water levels [Pequignot *et al.*, 2009], cross-shore modes tend to be observed on the reef flat. Otherwise, varying water level may detune the modal generation. Moreover, the frequency content of the envelope forcing affects the dominant EOF mode selected as described in section 3.1 for ROI and IPL. When the spectrum of the envelope forcing is weak near the theoretical $n=0$ mode frequency and energetic near the theoretical $n=1$ mode frequency, the dominant ($j=0$) EOF resembles the theoretical $n=1$ mode (e.g., record 777 for ROI and record 50 for IPL; see also Figure 6 bottom plots).

4.4. Theoretical Prediction of H_{ig}

The linear analytical model of section 4.1 and the Appendix A provide a one parameter prediction of the free surface elevation on the reef flat given empirical breaking parameters from the setup analyses, the water level on the reef flat, and the spectral content of the breaking wave height. The modal amplitudes of the free surface elevation, $\tilde{\eta}_n^{(c)}$, are governed by a damped, forced oscillator equation (7), and the results of section 3.1 suggest keeping only the first two modes in (14) in the prediction

$$\tilde{\eta}(x, t) = \sum_{n=0}^1 \mathcal{F}^{-1}[\hat{\eta}_n(x, \omega)]. \quad (18)$$

The results of sections 4.2 and 4.3 suggest that the forcing in (7) may be obtained from the shoaled envelope of the reef face free surface elevation (16), the water level on the reef flat h_r , the breaking, and shoaling parameters, γ_b and s_b from the setup analysis of Becker *et al.* [2014], the reef length L and the constant dissipation parameter \mathcal{D} . Figure 12 presents scatter plots of the observed H_{ig} at the sensor closest to the shoreline for the data described in Table 1 versus those predicted from (18), \tilde{H}_{ig} (4 times the standard deviation of $\tilde{\eta}(x_s, t)$), at the same location as the observations colored with the reef flat water level. The r^2 correlation coefficients between predicted \tilde{H}_{ig} and observed H_{ig} are 0.75 (ROI), 0.78 (CMI), 0.94 (IPG), 0.87 (IPL), 0.88 (IPN), and 0.97 (SAI). In Figure 2 and the accompanying text in section 2, we describe the correlations between observed H_{ig} and reef face wave height, H_f . Comparing Figures 2 and 12, we find that for ROI and IP in particular, the linear analytical model provides better predictions of H_{ig} than simply regressing on H_f and also provides a dynamical framework for the IG variability. Specifically, the theory relies on a wave breaking parameterization consistent with the setup analysis of Becker *et al.* [2014], and knowledge of the spectral characteristics of the envelope of the free surface elevation at breaking. We find the linear analytical model, (18), provides a better estimate of the largest observed values of H_{ig} for IP where the water level on the reef flat, h_r , is setup dominated, and dissipation is more important than for ROI and CMI. As shown in Figure 11, for ROI and CMI with tidally-dependent reef flat water levels, some history dependence to H_{ig} is exhibited that is not captured in the present linear analytical model and that appears to contribute to underpredicting the largest observed values of H_{ig} . For CMI, we also emphasize that two-dimensional effects that are neglected in the present work may be important for some large IG events. Finally, as described in section 2, the high values of r^2 obtained for IPG and SAI are in part due to the data analyzed only capturing a single large wave event (tropical storm ManYi).

Our prediction of the reef flat free surface elevation, $\tilde{\eta}(x, t)$, and \tilde{H}_{ig} includes a single tunable parameter, \mathcal{D} , which we interpret as a measure of the relative dissipation among the four sites. We find that values of \mathcal{D} increasing from ROI to SAI provide good estimates of H_{ig} using the parameters of Table 2. We remark, however, that the specific values of \mathcal{D} that provide agreement between observations and predictions of the shoreline IG wave height depend on the choice of L , γ_b and s_b in the forcing term of (7). The values of \mathcal{D} here were chosen so that the slope of the regression between the predicted and observed IG wave heights

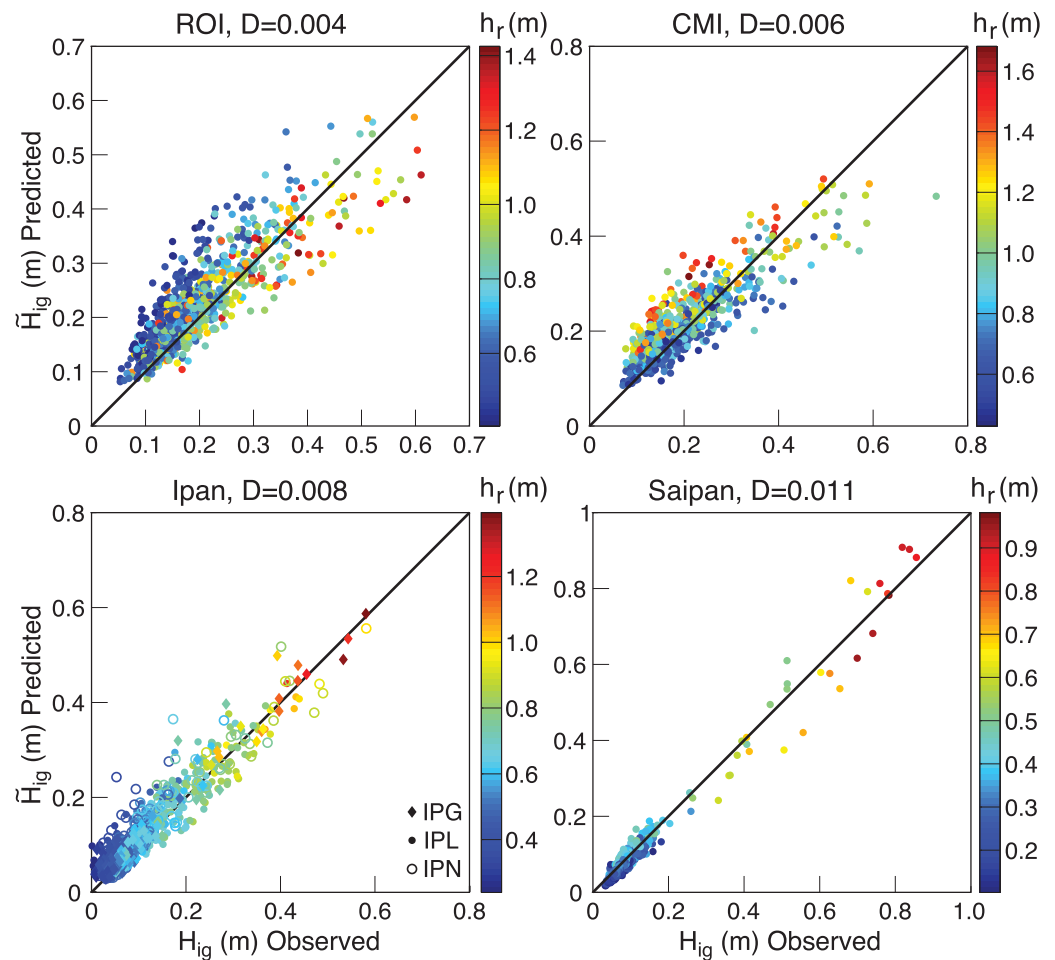


Figure 12. Observed versus predicted shoreline IG wave heights for all sites colored with the reef flat water level, h_r . The predicted \tilde{H}_{ig} was obtained from 4 times the standard deviation of $\tilde{\eta}$ from (18) using the parameters of Table 2.

was ~ 1 . Figure 10 also shows for ROI, $D=0.004$ gives reasonable agreement between the theoretical transfer function, (13), and the observed transfer function (17) at the shoreline. Measurements of reef flat roughness would be useful to determine the validity of the relative ranking of the dissipative parameter in the theory.

The data sets analyzed here also provide the opportunity to assess the effect of the reef length on IG generation during a large wave event. Tropical storm ManYi impacted both IPG and SAI with reef lengths of $L \sim 420$ and 135 m, respectively. For IPG ($L \sim 420$ m), the largest H_{ig} for the ~ 2 h record observed 30 m from the shoreline was ~ 0.6 m when the incident wave conditions were $H_f=3.9$ m, $T_p=11$ s and reef flat water level $h_r=1.39$ m (9 July 04:00, 2007). For SAI ($L \sim 135$ m), the largest H_{ig} observed at the midreef flat sensor located ~ 65 m from the shoreline was ~ 0.9 m, when $H_f=2.4$ m, $T_p=10$ s, and $h_r=0.95$ m (9 July 06:00, 2007). Further, when extrapolated to the shoreline using the mode 0 spatial profile ((1), with $n=0$), the observed H_{ig} at IPG is unchanged, while at SAI, H_{ig} increases to ~ 1.2 m, demonstrating that IG motions may be strongly amplified on shorter reefs.

5. Discussion

The linear analytical model of section 4 provide a prediction of the reef flat free surface elevation given the envelope of the incident free surface elevation, the reef flat water level and breaking and shoaling parameters derived from analyses of the setup. Equations (A1) and (A2) may be combined to obtain a forced, damped wave equation

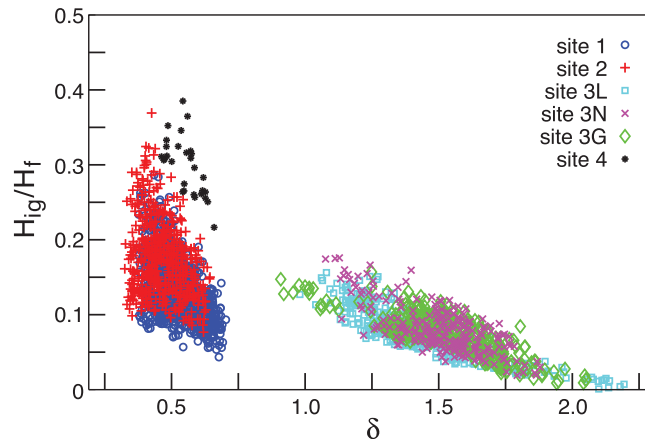


Figure 13. Observed shoreline IG wave height normalized by the observed reef face wave height, H_{ig}/H_f , versus $\delta = DL/\sqrt{gh_r}$ for all sites and $H_f > 1$ m.

for $\delta \gg 1$. For the reefs considered here, and for incident wave heights, $H_f > 1$ m, we find values of δ ranging from 0.4 to 0.7 for ROI, 0.3 to 0.6 for CMI, 0.9 to 2.2 for IP, and 0.5 to 0.7 for SAI suggesting that the reef flat variability at ROI, CMI, and SAI is wave-like, and at IP more dissipative. Figure 13 presents the observed shoreline IG wave height nondimensionalized by the reef face SS wave height, $H_{ig*} = H_{ig}/H_f$ when $H_f > 1$ m, as a function of δ . The dimensionless shoreline IG wave heights, H_{ig*} , for ROI, CMI, and SAI are largely independent of δ except potentially at the largest values of δ . For IP, the H_{ig*} are a decreasing function of δ consistent with more dissipative behavior.

For all four sites, the linear analytical model is able to capture a significant percentage of the variability of the IG significant wave height at the shoreline over a range of conditions without the need for a computationally expensive numerical model. We also demonstrate that for the reefs considered, the IG variability may be interpreted as dynamic setup as the linear analytical model follows from extending the breakpoint forcing of the mean motion (the setup) to the low-frequency band using the envelope of the observed SS free surface elevation. While knowledge of the spectral characteristics of the envelope of the reef face wave height is needed to force the model, as well as empirical shoaling and breaking parameters derived from the setup, it is encouraging that a linear analytical model is able to provide reasonable predictions of IG shoreline wave heights. Further, interpreting the observations in the context of the linear analytical model used here demonstrates that IG motions on steep reefs with small values of δ (wave-like) are more energetic and show more variability than those with large values of δ (dissipative). In addition, this study provides an estimate of low-frequency wave energy at fringing reef shorelines for inundation assessments. Finally, we remark that the present observational study complemented by the linear analytical model provides insight into the dynamics of IG generation for steep reefs, which in turn complements studies based on more sophisticated numerical models [e.g., Quataert *et al.*, 2015].

Appendix A: Derivation of (4) of Merrifield *et al.* [2014]

We consider linear forced, damped, long waves over an idealized step reef with the shoreline located at $x=0$, and the reef edge at $x=L$. The dynamics are those of Symonds *et al.* [1982] with linear dissipation,

$$\frac{\partial U}{\partial t} + g \frac{\partial \eta}{\partial x} = -\frac{1}{\rho h} \frac{\partial S_{xx}}{\partial x} - \mathcal{D}U \quad (\text{A1})$$

$$\frac{\partial \eta}{\partial t} + h_r \frac{\partial U}{\partial x} = 0 \quad (\text{A2})$$

where U is the depth integrated horizontal velocity, η is the free surface elevation, S_{xx} is the radiation stress, \mathcal{D} is a constant damping rate, h_r is the total water level over the reef flat assumed constant, and (x, t) are the cross shore coordinate and time, respectively. The linear damping rate, \mathcal{D} , may be related to the drag

coefficient C_d following *Symonds et al.* [1995] and *Monismith* [2007], $\mathcal{D}U \sim C_d \overline{|u|} / h_r$, where u is the instantaneous near-bed cross-shore velocity. In the radiation stress gradient term, the water level h is variable as the gradient is evaluated on the reef face in the limit as the reef face slope tends to infinity. The boundary conditions for free, undamped motions are

$$U=0, \quad \frac{\partial \eta}{\partial x}=0, \quad x=0 \quad (\text{A3})$$

$$\frac{\partial U}{\partial x}=0, \quad \eta=0, \quad x=L. \quad (\text{A4})$$

We decompose the IG motions into free spatial modes using finite Fourier cosine and sine transforms defined as

$$\bar{f}^{(c)}(k_n, t) = \int_0^L f(x, t) \cos(k_n x) dx \quad (\text{A5})$$

$$f(x, t) = \frac{2}{L} \sum_0^\infty \bar{f}^{(c)}(k_n, t) \cos(k_n x) \quad (\text{A6})$$

and

$$\bar{f}^{(s)}(k_n, t) = \int_0^L f(x, t) \sin(k_n x) dx \quad (\text{A7})$$

$$f(x, t) = \frac{2}{L} \sum_0^\infty \bar{f}^{(s)}(k_n, t) \sin(k_n x) \quad (\text{A8})$$

where k_n is defined in (2).

Taking the sine transform of (A1) and cosine transform of (A2), invoking (A3 and A4) and neglecting integrated terms with respect to the boundary terms in the forcing yields

$$\frac{\partial \bar{U}_n^{(s)}}{\partial t} - g k_n \bar{\eta}_n^{(c)} + \mathcal{D} \bar{U}_n^{(s)} = (-1)^{n+1} \left[\frac{1}{\rho h} S_{xx} \right]_{x=L} \quad (\text{A9})$$

$$\frac{\partial \bar{\eta}_n^{(c)}}{\partial t} + k_n h_r \bar{U}_n^{(s)} = 0 \quad (\text{A10})$$

where $(\bar{U}_n^{(s)}, \bar{\eta}_n^{(c)}) \equiv (\bar{U}^{(s)}(k_n, t), \bar{\eta}^{(c)}(k_n, t))$. We assume that breaking occurs on the reef face at a location $x=x_b$ in the limit where $x_b \rightarrow L$. Invoking the shallow water approximation for the radiation stress, we obtain

$$\left(\frac{1}{\rho h} S_{xx} \right)_{x=L} = \frac{3}{32} g \gamma_b H_b(t) \quad (\text{A11})$$

where

$$\gamma_b = \frac{H_b}{h_b}$$

is the ratio of breaking (significant) wave height, H_b , to the water depth, h_b , at breaking. In *Becker et al.* [2014], the mean (15 min average) H_b and h_b were determined from the observations of wave height and setup assuming conservative shoaling and a point break model. For the setup analysis, the 15 min average H_b was highly correlated with the reef face wave height, H_r , and γ_b was a site specific, tidally-dependent breaking parameter. We describe in section 4.2 how we estimate a time dependent breaking wave height, $H_b(t)$, in (A11) from the observations of incident reef face wave height and breaking wave setup.

Combining (A9) and (A10) to eliminate $\bar{U}_n^{(s)}$ and invoking (A11), we obtain a forced, damped oscillator equation (7) for the time-dependent modal amplitude, $\bar{\eta}_n^{(c)}$. In physical (x, t) space, (7) is a forced, damped long wave equation (see (19)).

Acknowledgments

This work was supported through a grant from the National Science Foundation (OCE-0927407). Support for the Guam field experiment was provided by the U. S. Army Corps of Engineers via a subcontract through the University of California, San Diego as part of the PILOT project. Chris Kontoes, Carly Quisenberry, and Derek Young planned and executed the RMI field experiments. Additional field support was provided by Murray Ford, Christine Pequignet, Paul Lethaby, Tyson Hilmer, Kimball Millikan, Lauren Tuthill, Chris Colgrove, Melanie Hutchinson, Chris Ostrander, and Bryan Rahter. Don Hess at the College of the Marshall Islands and Jeff Pleadwell at Ipan, Guam provided logistical support. Jason Miller of the University of Guam Marine Laboratory provided invaluable assistance with the diving operation at Ipan. Anna Merrifield, Nicole Deyerl, and Sarah Yasui assisted with the data processing. The data sets from Ipan used in this study are available through the USACE at <http://www.frf.usace/army/mil/pilot/pilot.shtml>. Data sets from ROI, CMI, and SAI used in this study are available upon request (jbecker@soest.hawaii.edu).

References

- Baldock, T. E. (2006), Long wave generation by the shoaling and breaking of transient wave groups on a beach, *Proc. R. Soc. A* **462**, 1853–1876, doi:10.1098/rspa.2005.1642.
- Becker, J. M., M. A. Merrifield, and M. Ford (2014), Water level effects on breaking wave setup for Pacific Island fringing reefs, *J. Geophys. Res. Oceans*, **119**, 914–932, doi:10.1002/2013JC009373.
- Ford, M. R., J. M. Becker, and M. A. Merrifield (2012), Reef flat wave processes and excavation pits: Observations and implications for Majuro Atoll, Marshall Islands, *J. Coastal Res.*, **29**(3), 545–554.
- Lo, J. (1988), Dynamic wave setup, *Coastal Eng. Proc.*, **1**(21), 999–1010.
- Lugo-Fernandez, A., H. H. Roberts, W. J. Wiseman Jr., and B. L. Carter (1998), Water level and currents of tidal and infra gravity periods at Tague Reef, St. Croix (USVI), *Coral Reefs*, **17**, 343–349.
- Ma, G., S.-F. Su, S. Liu, and J.-C. Chu (2014), Numerical simulation of infragravity waves in fringing reefs using a shock-capturing non-hydrostatic model, *Ocean Eng.*, **85**, 54–64.
- Merrifield, M. A., J. M. Becker, M. Ford, and Y. Yao (2014), Observations and estimates of wave-driven water level extremes at the Marshall Islands, *Geophys. Res. Lett.*, **41**, 7245–7253, doi:10.1002/2014GL061005.
- Monismith, S. G. (2007), Hydrodynamics of coral reefs, *Annu. Rev. Fluid Mech.*, **39**(1), 37–55.
- Nakaza, E., and M. Hino (1991), Bore-like surf beat in a reef zone caused by wave groups of incident short period waves, *Fluid Dyn. Res.*, **7**, 89, doi:10.1016/0169-5983(91)90062-N.
- Nwogu, O., and Z. Demirbilek (2010), Infragravity wave motions and runup over shallow fringing reefs, *J. Waterway, Port Coastal Ocean Eng.*, **136**, 295–305.
- Pequignet, A.-C., J. M. Becker, M. A. Merrifield, and J. Aucan (2009), Forcing of resonant modes on a fringing reef during tropical storm Man-Yi, *Geophys. Res. Lett.*, **36**, L03607, doi:10.1029/2008GL036259.
- Pequignet, A.-C. N., J. M. Becker, and M. A. Merrifield (2014), Energy transfer between wind waves and low-frequency oscillations on a fringing reef, Ipan, Guam, *J. Geophys. Res. Oceans*, **119**, 6709–6724, doi:10.1002/2014JC010179.
- Pomeroy, A., R. Lowe, G. Symonds, A. Van Dongeren, and C. Moore (2012), The dynamics of infragravity wave transformation over a fringing reef, *J. Geophys. Res.*, **117**, C11022, doi:10.1029/2012JC008310.
- Quataert, E., C. Storlazzi, A. van Rooijen, O. Cheriton, and A. van Dongeren (2015), The influence of coral reefs and climate change on wave-driven flooding of tropical coastlines, *Geophys. Res. Lett.*, **42**, 6407–6415, doi:10.1002/2015GL064861.
- Sheremet, A., R. T. Guza, S. Elgar, and T. H. C. Herbers (2002), Observations of nearshore infragravity waves: Seaward and shoreward propagating components, *J. Geophys. Res.* **107**(C8), 3095, doi:10.1029/2001JC000970.
- Sheremet, A., T. Staples, F. Ardhuin, S. Suanez, and B. Fichaut (2014), Observations of large infragravity wave runup at Banneg Island, France, *Geophys. Res. Lett.*, **41**, 976–982, doi:10.1002/2013GL058880.
- Su, S.-F., G. Ma, and T.-W. Tsu (2015), Boussinesq modeling of spatial variability of infragravity waves on fringing reefs, *Ocean Eng.*, **101**, 78–92, doi:10.1016/j.oceaneng.2015.04.022.
- Symonds, G., D. A. Huntley, and A. J. Bowen (1982), Two-dimensional surf beat: Long wave generation by a time-varying breakpoint, *J. Geophys. Res.*, **87**(C1), 492–498, doi:10.1029/JC087iC01p00492.
- Symonds, G. K. P. Black, and I. R. Young (1995), Wave-driven flow over shallow reefs, *J. Geophys. Res.*, **100**(2), 639–648, doi:10.1029/94JC02736.
- Torres-Freyermuth, A., I. Marino-Tapia, C. Coronado, P. Salles, G. Medellin, A. Pedrozo-Acuna, R. Silva, J. Candela, and R. Igelesias-Preto (2012), Wave-induced extreme water levels in the Puerto Morelos fringing reef lagoon, *Nat. Hazards Earth Syst. Sci.*, **12**, 3765–3773.
- Van Dongeren, A., R. Lowe, A. Pomeroy, D. M. Tranh, D. Roelvink, G. Symonds, and R. Ranasinghe (2013), Numerical modeling of low-frequency wave dynamics over a fringing coral reef, *Coastal Eng.*, **73**, 178–190.
- Vetter, O., J. M. Becker, M. A. Merrifield, A.-C. Pequignet, J. Aucan, S. Boc, and C. Pollard (2010), Wave set-up over a Pacific Island fringing reef, *J. Geophys. Res.*, **115**, C12066, doi:10.1029/2010JC006455.
- Winant, C. D., D. L. Inman, and C. E. Nordstrom (1975), Description of seasonal beach changes using empirical eigenfunctions, *J. Geophys. Res.*, **80**(15), 1979–1986, doi:10.1029/JC080i015p01979.
- Yao, Y., Z. Huang, S. G. Monismith, and E. Y. M. Lo (2012), Characteristics of monochromatic wave breaking over fringing reefs, *J. Coastal Res.*, **29**(1), 94–104.